

Design, Synthesis, and Evaluation of CF₃AuCNR Precursors for Focused Electron Beam Induced Deposition of Gold

Will G. Carden,^a Rachel M. Thorman,^b Ilyas Unlu,^b Khalil A. Abboud,^a D. Howard Fairbrother^b and Lisa McElwee-White^a

^aDepartment of Chemistry, University of Florida, Gainesville, Florida 32611-7200, USA

^bDepartment of Chemistry, Johns Hopkins University, Baltimore, Maryland 21218-2685, USA

lmwhite@chem.ufl.edu

Table of Contents

NMR Spectra.....	S-2
TGA Traces.....	S-6
X-ray Analysis.....	S-8
Mass Spectrometry.....	S-13
Estimated Local Temperature Increase During FEBID.....	S-16
EDS and AES of FEBID Deposits from CF₃AuCNRMe.....	S-19
References.....	S-20

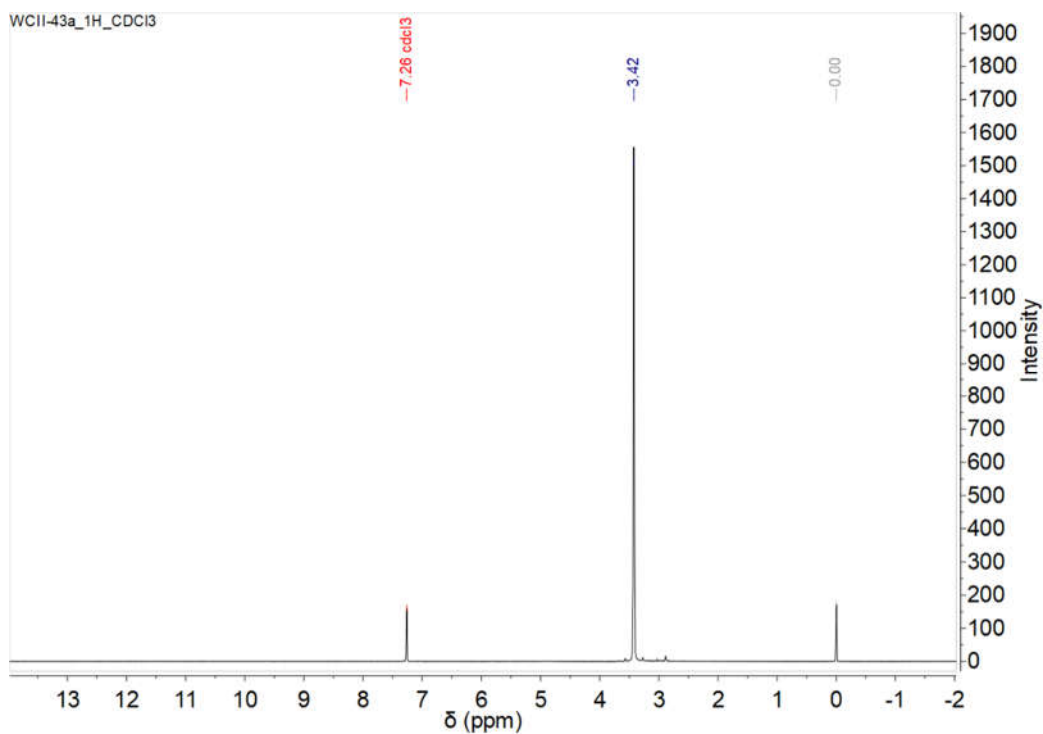


Figure S1. ^1H NMR spectrum of **1a** in CDCl_3 .

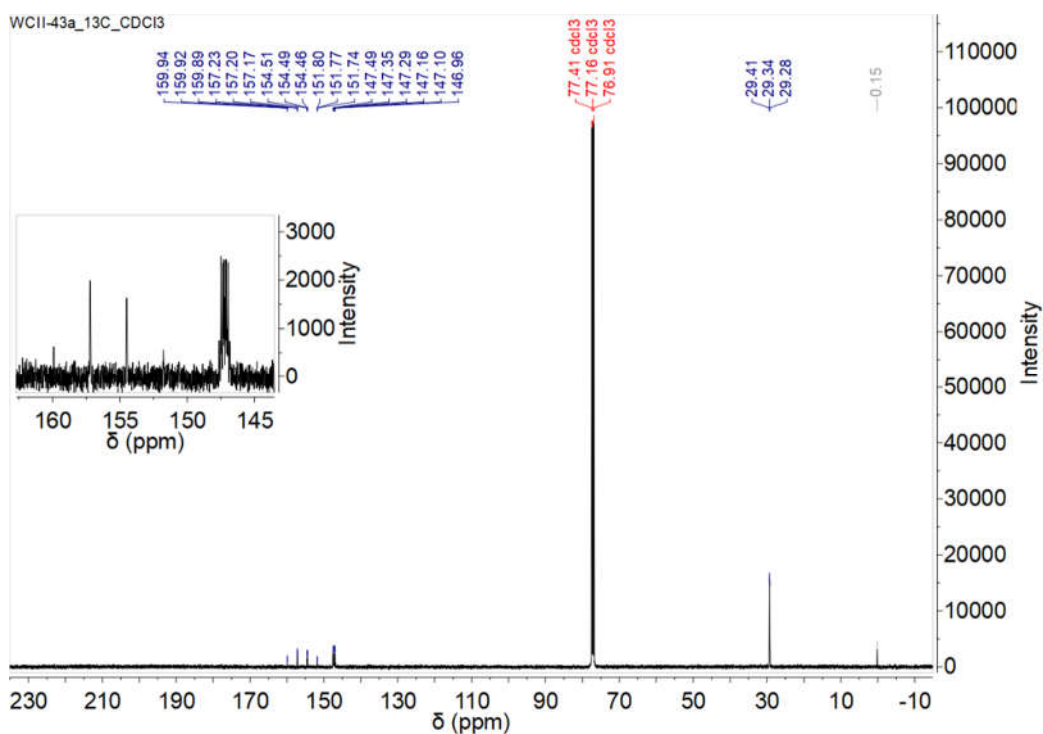


Figure S2. ^{13}C NMR spectrum of **1a** in CDCl_3 ; inset: enhanced view of the two resonances in the ca. δ 145-160 ppm region.

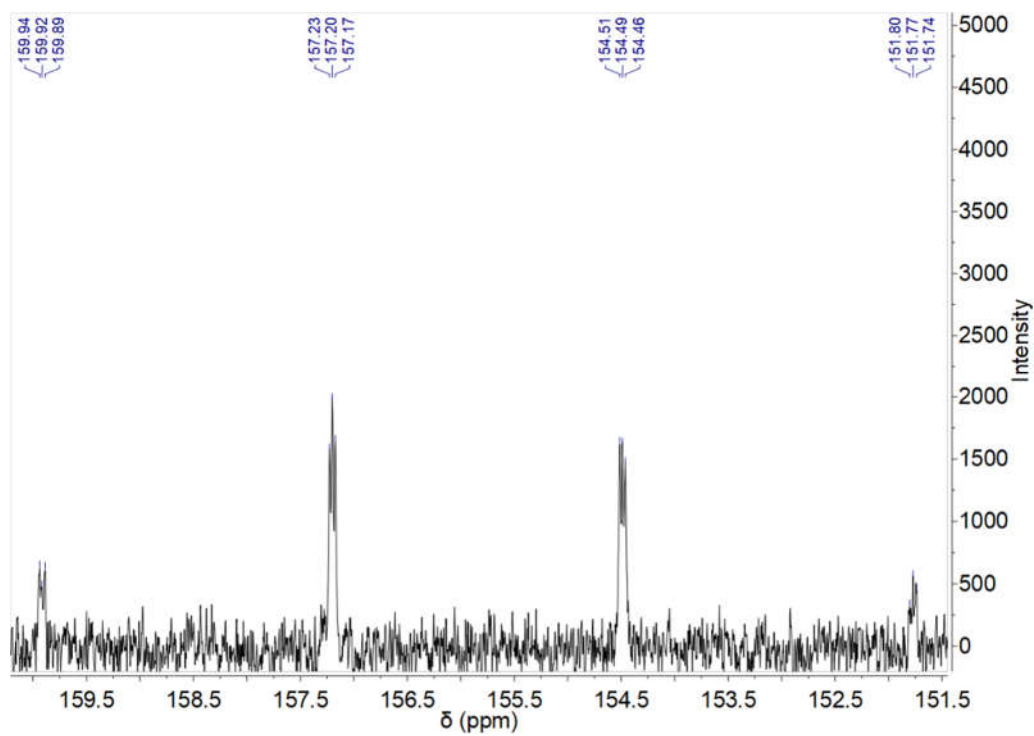


Figure S3. Enhanced view of the qt in the ^{13}C NMR spectrum of **1a** in CDCl_3 .

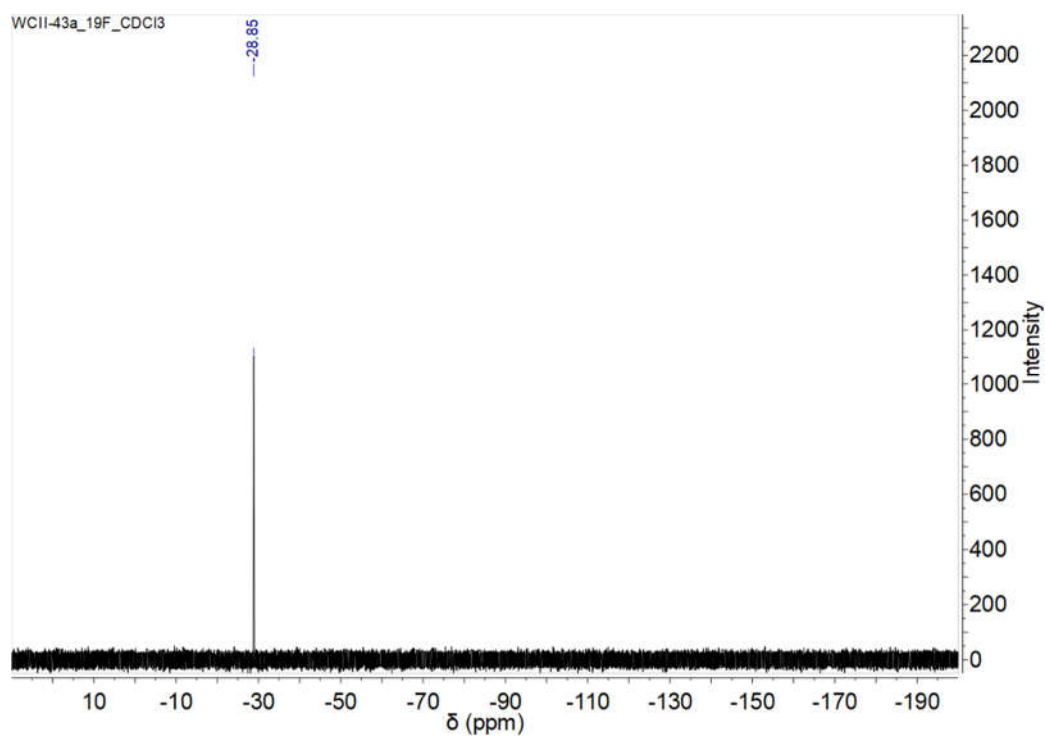


Figure S4. ^{19}F NMR spectrum of **1a** in CDCl_3 .

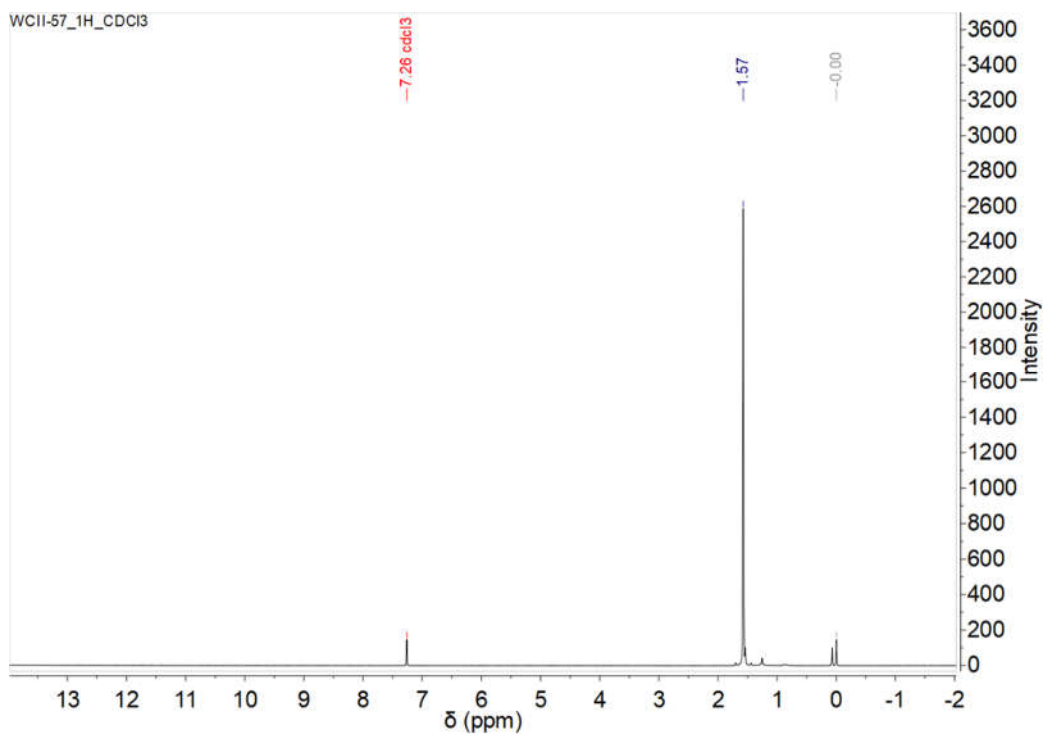


Figure S5. ^1H NMR spectrum of **1b** in CDCl_3 .

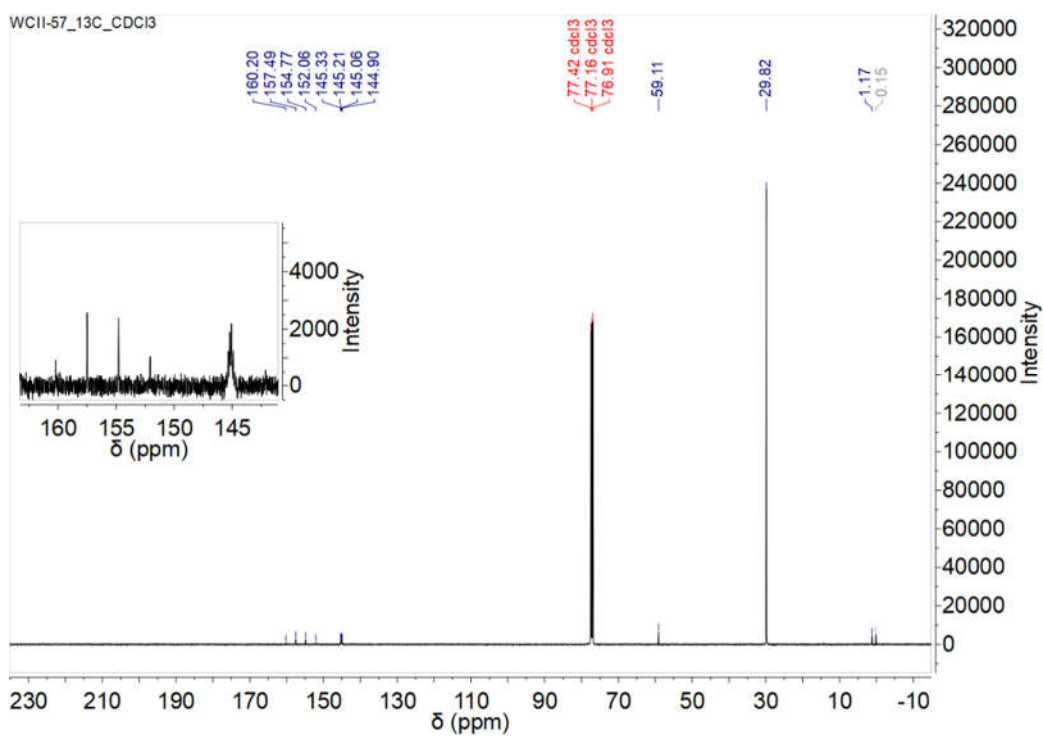


Figure S6. ^{13}C NMR spectrum of **1b** in CDCl_3 ; inset: enhanced view of the two resonances in the ca. δ 145-160 ppm region.

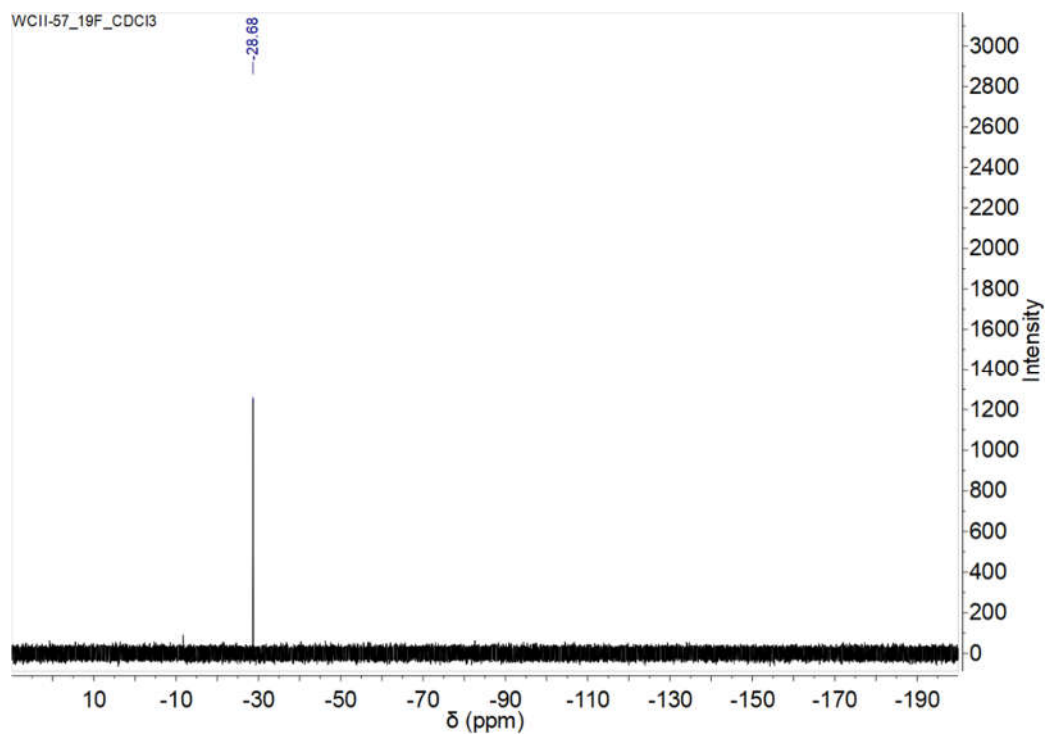


Figure S7. ^{19}F NMR spectrum of **1b** in CDCl_3 .

Thermogravimetric Analysis

TGA experiments were conducted on a TA Discovery5500 instrument and were performed under N₂ gas.

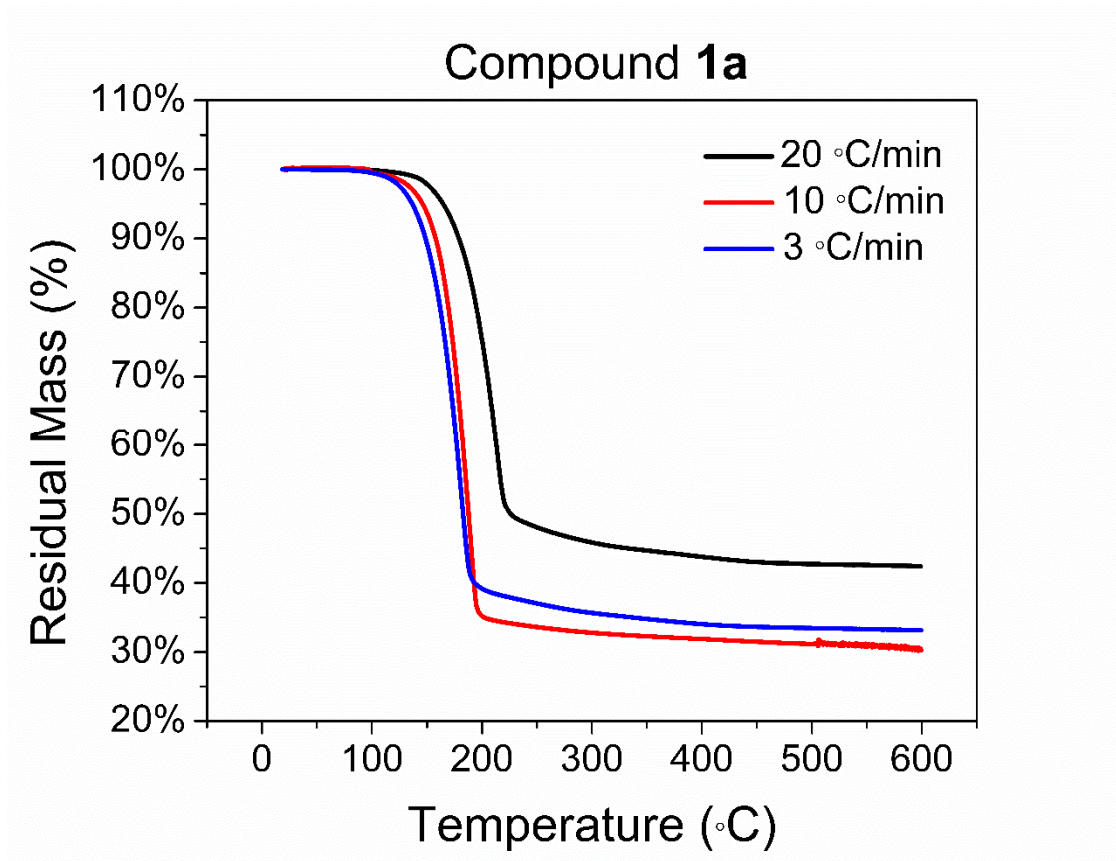


Figure S8. TGA traces for compound **1a** with varying ramp rates as denoted in the legend. For ramp rates of 3 and 10 °C/min, the residual mass from 200-600 °C (35-40%) is less than that of metallic gold (64%) in **1a** and, therefore, suggestive of competing sublimation and decomposition. Likewise, for the ramp rate of 20 °C/min, the residual mass between 250-600 °C (43-48%) is also indicative of competing sublimation and decomposition. However, the higher residual mass relative to that of the slower ramp rates suggests that more decomposition occurs at faster ramp rates.

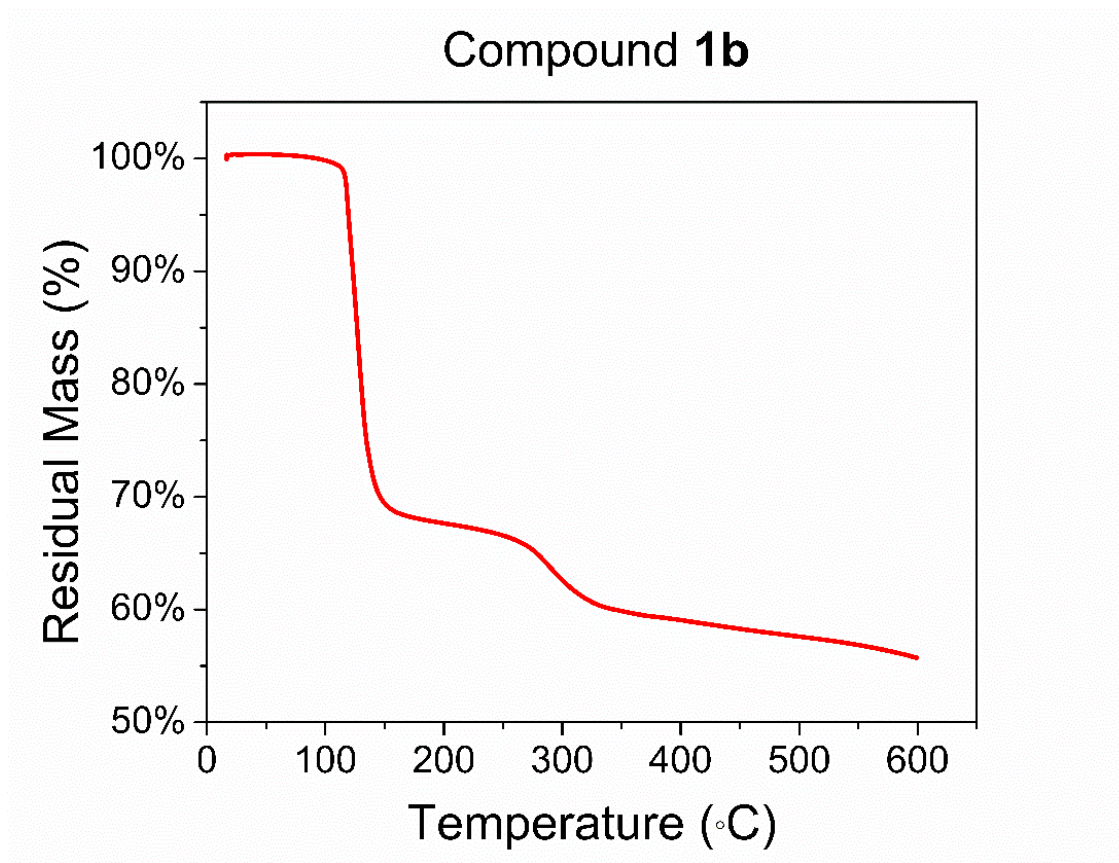


Figure S9. TGA trace for compound **1b** with a ramp rate of 10 °C/min. The residual mass at 500-600 °C (55-58%) is suggestive of complete decomposition of **1b** to gold metal.

X-ray Crystallography Experimental Methods and Structure Refinement for 1a

Single-Crystal X-ray Diffraction of 1a. X-Ray Intensity data were collected at 100 K on a Bruker **DUO** diffractometer using MoK α radiation ($\lambda = 0.71073 \text{ \AA}$) and an APEXII CCD area detector. Raw data frames were read by the program SAINT¹ and integrated using 3D profiling algorithms. The resulting data were reduced to produce hkl reflections and their intensities and estimated standard deviations. The data were corrected for Lorentz and polarization effects and numerical absorption corrections were applied based on indexed and measured faces. The structure was solved and refined in *SHELXTL2014*,¹ using full-matrix least-squares refinement. The non-H atoms were refined with anisotropic thermal parameters and all of the H atoms were calculated in idealized positions and refined riding on their parent atoms. The molecule is located on a mirror plane where only one F atom lies outside of it; thus, the unit cell consists of four molecules. In the final cycle of refinement, 12460 reflections (of which 1149 are observed with $I > 2\sigma(I)$) were used to refine 48 parameters and the resulting R_1 , wR_2 and S (goodness of fit) were 1.05%, 2.65% and 1.26, respectively. The refinement was carried out by minimizing the wR_2 function using F^2 rather than F values. R_1 is calculated to provide a reference to the conventional R value but its function is not minimized. All figures pertaining to X-ray crystallography were generated using Mercury CSD version 3.8 (Build RC2). Figures generated for previously reported structures (**1b** and **2a**) were obtained using the corresponding cif file which was exported from the CCDC ConQuest application.

Table S1. Atomic coordinates ($\times 10^4$) and equivalent isotropic displacement parameters ($\text{\AA}^2 \times 10^3$) for **1a**. $U(\text{eq})$ is defined as one third of the trace of the orthogonalized U^{ij} tensor.

	x	y	z	$U(\text{eq})$
Au1	2960(1)	5000	4401(1)	13(1)
F1	3725(1)	5000	9371(3)	20(1)
F2	4389(1)	6856(3)	7067(2)	26(1)
C1	3901(2)	5000	7101(5)	16(1)
C2	2103(2)	5000	1607(5)	16(1)
N1	1627(1)	5000	-45(5)	16(1)
C3	998(2)	5000	-2030(5)	20(1)

Table S2. Bond lengths [Å] and angles [°] for **1a**.

Au1-C2	1.988(3)
Au1-C1	2.047(3)
F1-C1	1.367(3)
F2-C1	1.371(2)
C1-F2#1	1.371(2)
C2-N1	1.144(4)
N1-C3	1.435(4)
C3-H3A	0.9800
C3-H3B	0.9800
C3-H3C	0.9800
C2-Au1-C1	175.74(11)
F1-C1-F2#1	103.81(16)
F1-C1-F2	103.81(16)
F2#1-C1-F2	104.2(2)
F1-C1-Au1	116.03(18)
F2#1-C1-Au1	113.81(14)
F2-C1-Au1	113.81(14)
N1-C2-Au1	177.9(2)
C2-N1-C3	176.8(3)
N1-C3-H3A	109.5
N1-C3-H3B	109.5
H3A-C3-H3B	109.5
N1-C3-H3C	109.5
H3A-C3-H3C	109.5
H3B-C3-H3C	109.5

Symmetry transformations used to generate equivalent atoms:

#1 x,-y+1,z

Table S3. Anisotropic displacement parameters ($\text{\AA}^2 \times 10^3$) for **1a**. The anisotropic displacement factor exponent takes the form: $-2\pi^2 [h^2 a^{*2}U^{11} + \dots + 2 h k a^* b^* U^{12}]$

	U^{11}	U^{22}	U^{33}	U^{23}	U^{13}	U^{12}
Au1	11(1)	14(1)	13(1)	0	1(1)	0
F1	27(1)	20(1)	13(1)	0	4(1)	0
F2	20(1)	31(1)	24(1)	5(1)	-2(1)	-12(1)
C1	14(1)	18(1)	14(1)	0	1(1)	0
C2	16(1)	14(1)	20(1)	0	4(1)	0
N1	15(1)	14(1)	19(1)	0	2(1)	0
C3	19(1)	21(1)	18(1)	0	-4(1)	0

Table S4. Hydrogen coordinates ($\times 10^4$) and isotropic displacement parameters ($\text{\AA}^2 \times 10^3$) for **1a**.

	x	y	z	U(eq)
H3A	564	4050	-1647	30
H3B	1188	4377	-3441	30
H3C	811	6573	-2357	30

Table S5. Selected hydrogen bonding parameters for **1a** (\AA) and (deg).

D-H \cdots A	d(D-H)	d(H \cdots A) ^a	d(D \cdots A)	$\angle(\text{DHA})$
C3-H3A \cdots F2#2	0.98	2.41	3.293(3)	149.9
C3-H3B \cdots F2#3	0.98	2.60	3.372(3)	136.2
C3-H3C \cdots F2#4	0.98	2.59	3.293(3)	129.1

Symmetry transformations used to generate equivalent atoms:

#1 x,-y+1,z #2 x-1/2,y-1/2,z-1 #3 -x+1/2,y-1/2,-z #4 x-1/2,-y+3/2,z-1

^aH \cdots A distances are reported without an esd as the H atoms are in idealized geometric positions

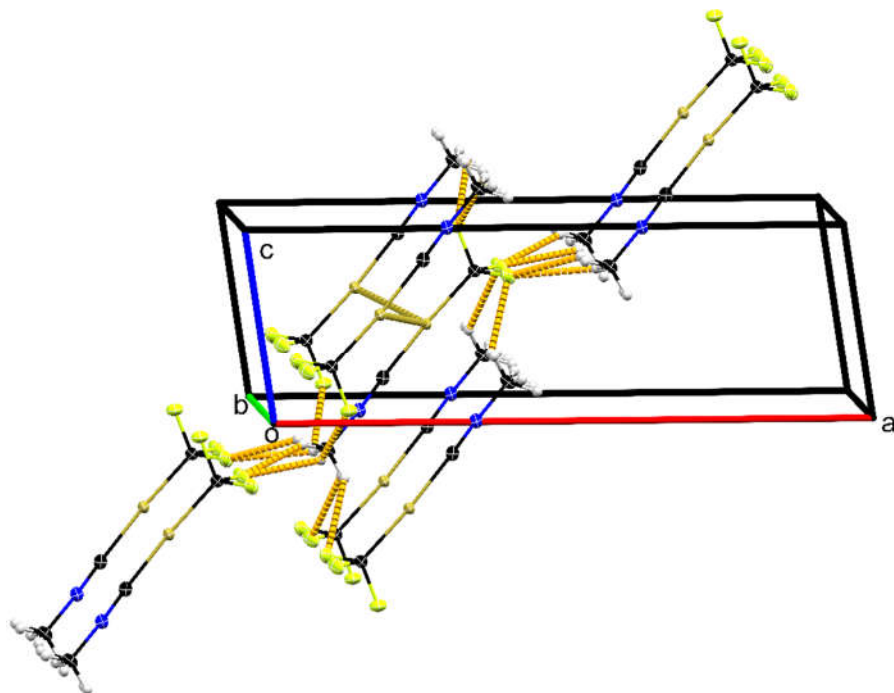


Figure S10. C-H \cdots F hydrogen bonding networks in **1a** shown in orange. Au-Au interactions are shown in gold for reference. Additional hydrogen bonding is present at slightly longer distances (> 2.7 Å) but is not shown for clarity.

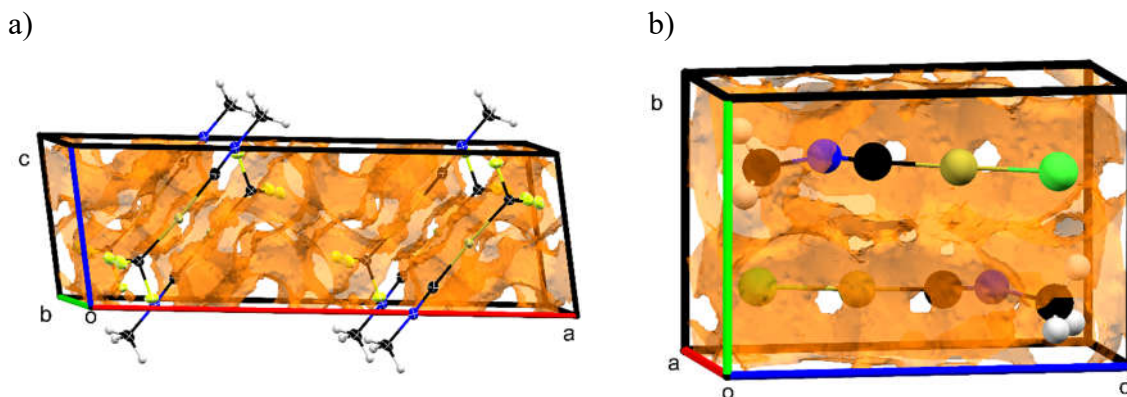


Figure S11. Void volume analysis for the unit cells of a) **1a** and b) **2a**. The void volume was determined by a probe with a radius of 0.2 Å and a grid spacing of 0.1 Å and is depicted by the orange spheres inside of each unit cell. The void volume in the unit cell of **1a** is approximately 137.97 Å³ or 24.6% of the unit cell. For **2a**, the void volume occupies approximately 63.88 Å³ or 27.8% of the unit cell. This suggests that XAuL molecules are packed more efficiently in the lattice of **2a** compared to **1a**.

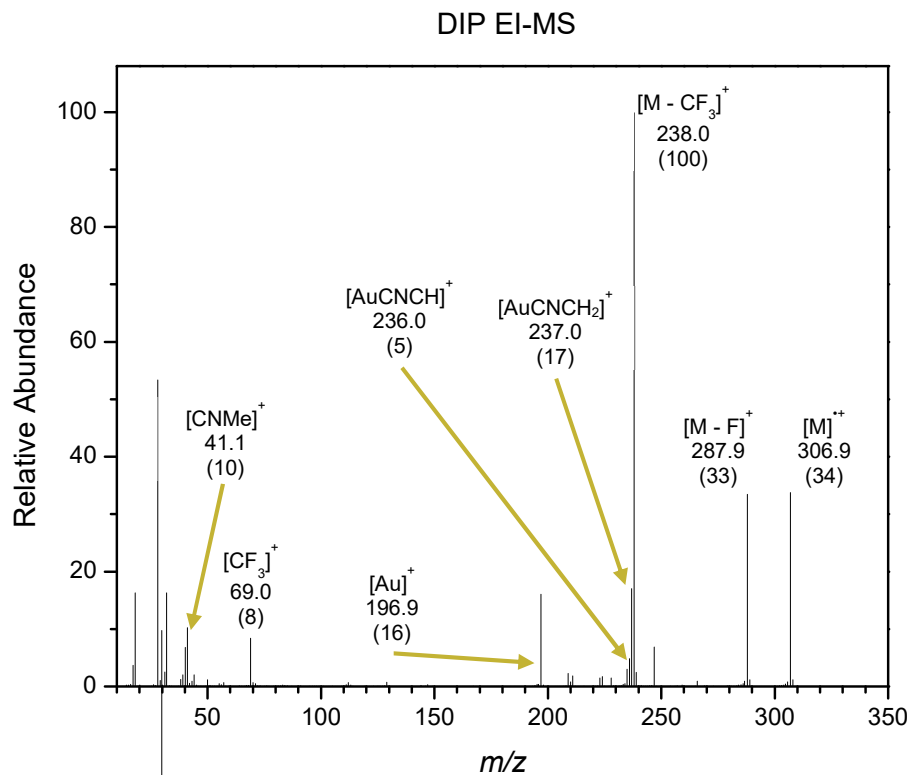


Figure S12. DIPEI mass spectrum of **1a**.

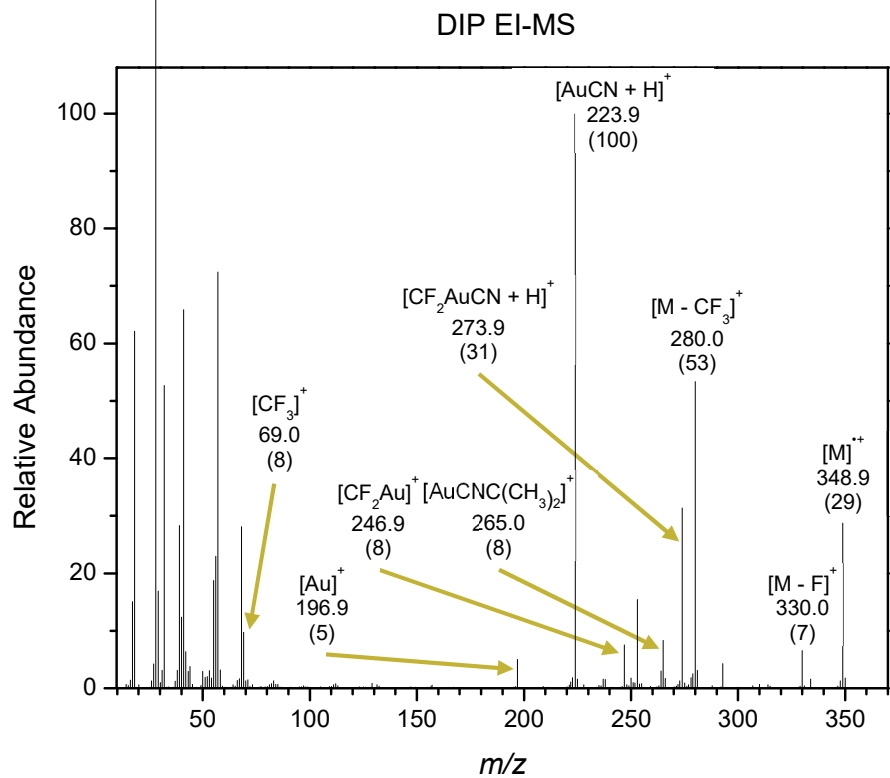


Figure S13. DIPEI mass spectrum of **1b**.

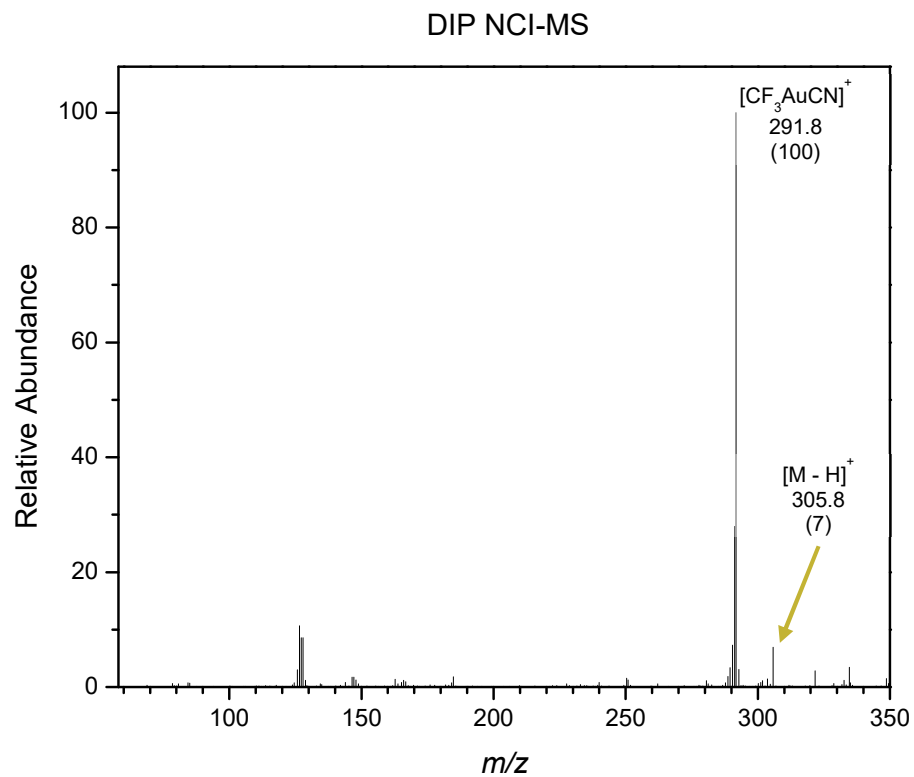


Figure S14. DIPNCI mass spectrum of **1a**.

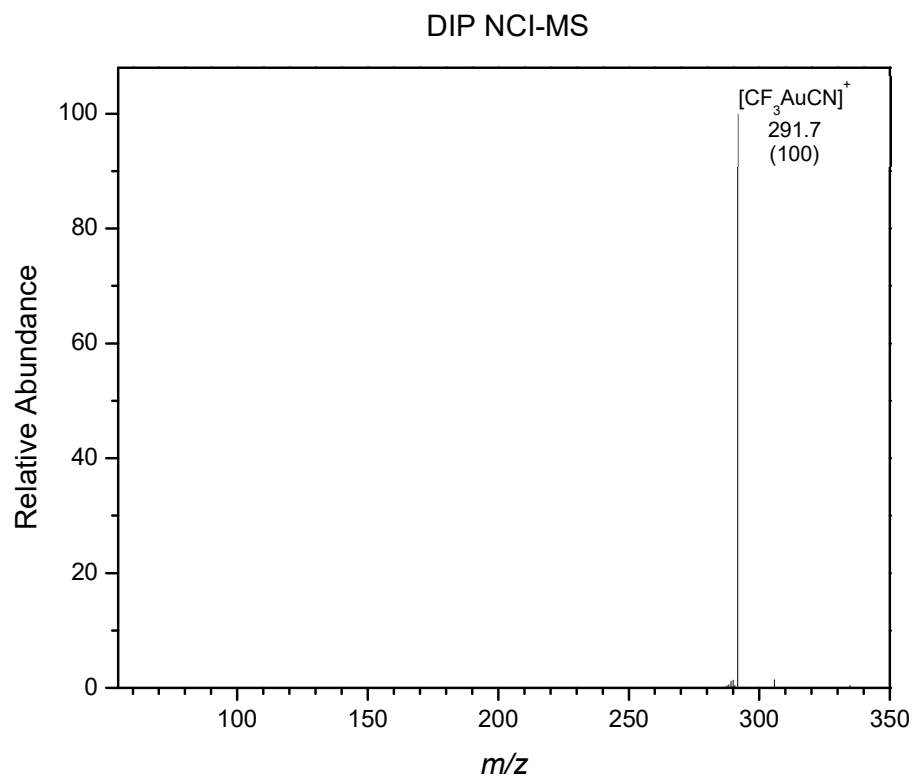


Figure S15. DIPNCI mass spectrum of **1b**.

Table S6. Selected CNR derived ions and their relative abundances as observed in positive ion DIPEI-MS of compounds **1a** and **1b**. Relative abundances $\geq 5\%$ are included.

EI Ions	<i>m/z</i> (1a)	abundance (1a)	<i>m/z</i> (1b)	abundance (1b)
[CNCH ₂] ⁺	40.1 (7)	7	n.o. ^b	n.o. ^b
[CNC(CH ₃) ₂] ⁺	n.o. ^b	n.o. ^b	68.0	28
[C(CH ₃) ₃] ⁺	n.o. ^b	n.o. ^b	57.1	72
[NC(CH ₃) ₂] ⁺	n.o. ^b	n.o. ^b	56.1	23
[NC(CH ₃)(CH ₂)] ⁺	n.o. ^b	n.o. ^b	55.1	19
[NC(CH ₃)] ⁺	n.o. ^b	n.o. ^b	41	66
[C(CH ₃)(CH ₂)] ⁺	n.o. ^b	n.o. ^b	40.1	12
[NC(CH ₂)] ⁺	n.o. ^b	n.o. ^b	39	28
[C(CH ₃)(CH)] ⁺	n.o. ^b	n.o. ^b	39	28
[C(CH ₂)(CH ₂)] ⁺	n.o. ^b	n.o. ^b	39	28
[NC(CH)] ⁺	n.o. ^b	n.o. ^b	39	28
[C(CH ₃)(C)] ⁺	n.o. ^b	n.o. ^b	39	28
EI Ions	<i>m/z</i> (1a)	abundance (1a) ^a	<i>m/z</i> (1b)	abundance (1b) ^b
[CNCH ₂] ⁺	40.1 (7)	7	n.o. ^b	n.o. ^c
[CNC(CH ₃) ₂] ⁺	n.o. ^c	n.o. ^c	68.0	28
[C(CH ₃) ₃] ⁺	n.o. ^c	n.o. ^c	57.1	72
[NC(CH ₃) ₂] ⁺	n.o. ^c	n.o. ^c	56.1	23
[NC(CH ₃)(CH ₂)] ⁺	n.o. ^c	n.o. ^c	55.1	19
[NC(CH ₃)] ⁺	n.o. ^c	n.o. ^c	41	66
[C(CH ₃)(CH ₂)] ⁺	n.o. ^c	n.o. ^c	40.1	12
[NC(CH ₂)] ⁺	n.o. ^c	n.o. ^c	39	28
[C(CH ₃)(CH)] ⁺	n.o. ^c	n.o. ^c	39	28
[C(CH ₂)(CH ₂)] ⁺	n.o. ^c	n.o. ^c	39	28
[NC(CH)] ⁺	n.o. ^c	n.o. ^c	39	28
[C(CH ₃)(C)] ⁺	n.o. ^c	n.o. ^c	39	28

^aNormalized to 238.0 *m/z* for **1a** and 223.9 *m/z* for **1b**.

^bNormalized to 223.9 *m/z* for **1b**.

^cn.o. = not observed.

Estimation of the Maximum Local Temperature Increase Experienced During FEBID

To estimate the maximum local temperature increases we could expect to see we have used the information contained in the detailed FEBID review written by Ivo Utke² as a starting point. In this review it states that in a situation where the beam diameter is smaller than the dimension of the excitation volume the maximum temperature increase experienced by a substrate which is being irradiated by an electron beam is given by ΔT in equation (1), where V is the acceleration voltage, I is the charged particle current, κ is the thermal conductivity of the bulk substrate and η represents the backscattered electron yield. R_E is equal to the projected range of incident electrons within the substrate as this represents the radius within which the energy is dissipated / heat is generated.

$$\Delta T (max) = \frac{V I (1 - \eta)}{\pi \kappa R_E} \quad (1)$$

This scenario is described by **Figure S16a**.

In the present experimental set up however, the size of the deposits are determined by the Auger electron beam which is several 10s of microns in size as shown in **Figure 5** in the main manuscript. Based on the SEM images shown in **Figure 5** we can see that the shape of the deposits is best described as an ellipse with major and minor axes of $\approx 50 \mu\text{m} \times 30 \mu\text{m}$. This scenario is described by **Figure S16b**.

For 3keV electrons (the primary electron energy used in this study) the value of R_E in silicon (the substrate used for deposition) is $\approx 400\text{nm}$.

Since R_E ($0.4 \mu\text{m}$) is much smaller than the two-dimensional axes of the deposits formed in the present study ($30 \times 50\mu\text{m}$) we can approximate the volume within which the electron energy is dissipated to be equivalent to an elliptical cylinder whose volume is given by; $V(\text{actual}) \approx 50 \mu\text{m} \times 30 \mu\text{m} \times 400 \text{ nm} \times \pi$ as shown in **Figure S16b**.

In contrast, when the impinging beam diameter is smaller than the dimension of the excitation volume (as it typically the case in FEBID) then the energy of the incident electron beam would be dissipated into a hemisphere of radius R_E as shown in **Figure S16a** with a volume given by:

$$V(\text{point source}) = 2/3 \times \pi \times R_E^3.$$

Using this information, we can compute an effective radius for our particular electron geometry by determining the effective R_E value ($R_E(\text{Effective})$) for a point source electron beam which gives rise to an excitation volume equal to the one generated using the beam size, in our experiments by using the equation:

$$V(\text{point source}) = V(\text{actual}).$$

So,

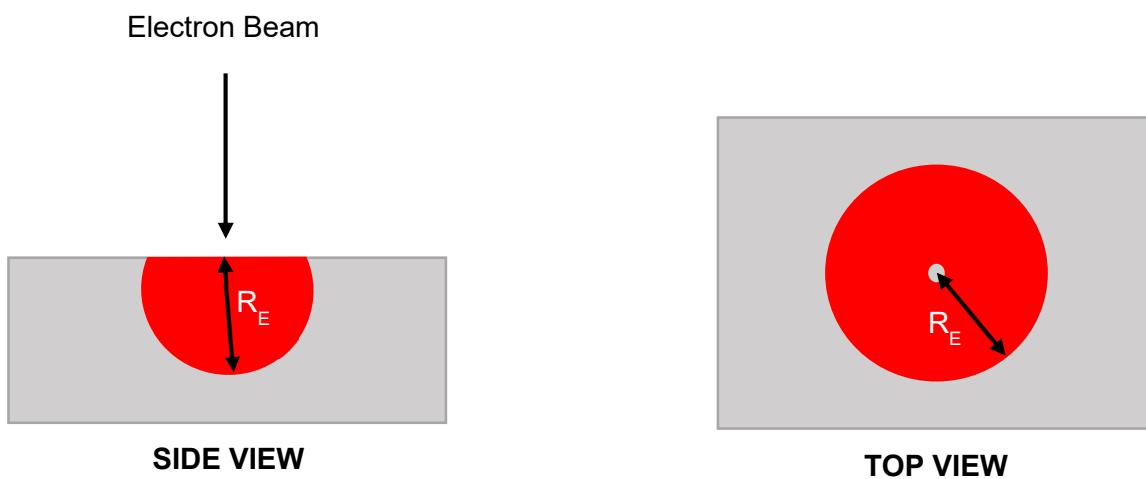
$$50 \mu\text{m} \times 30 \mu\text{m} \times 400 \text{ nm} \times \pi = 2/3 \times \pi \times R_{\text{E (Effective)}}^3$$

This leads to a determination of $R_{\text{E (Effective)}} = 9.7 \mu\text{m}$

If we assume that the backscattered electron yield is zero (worst case scenario in terms of the temperature increase a substrate could experience during electron irradiation) and use value of $V = 3 \text{ KeV}$, $I = 1 \times 10^{-6} \text{ A}$, and $\kappa = 130 \text{ W m}^{-1} \text{ }^\circ\text{C}$ (thermal conductivity of the Si substrate) then $\Delta T (\text{max}) = 0.8 \text{ }^\circ\text{C}$.

Although the detailed nature of the carbon deposited is undefined in the present study, the deposits contain significant quantities ($> 20 \text{ at. \%}$) of gold whose thermal conductivity is $310 \text{ W m}^{-1} \text{ }^\circ\text{C}$.

a) Typical FEBID Experiment



b) Current Experiment

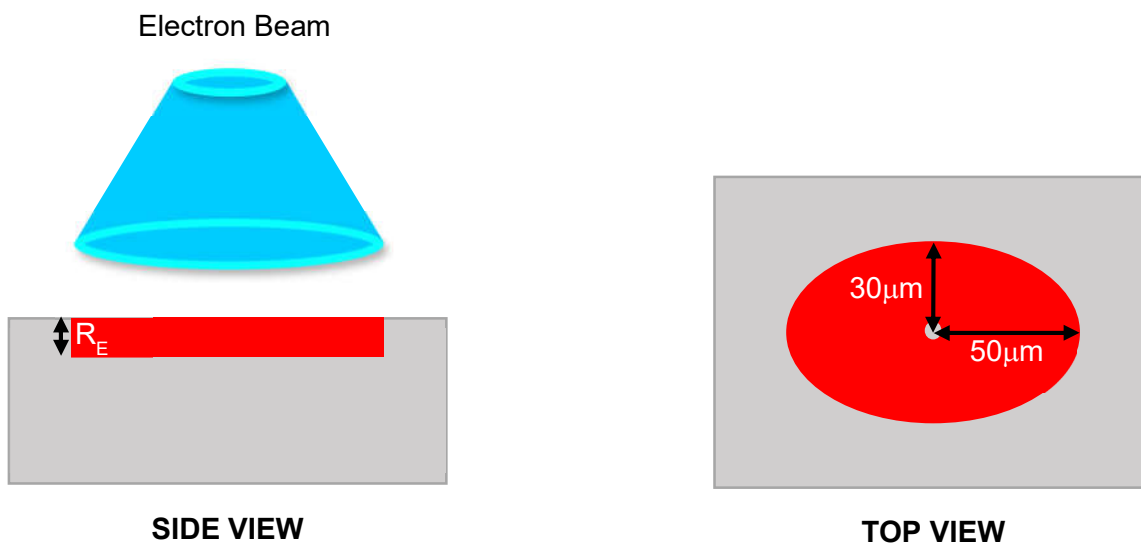


Figure S16. Electron-surface interaction volumes as described in a) typical FEBID experiments and b) the current experiment. The region shaded in red represents the volume within which the electron energy is dissipated.

Comparison of EDS and AES Data Acquired from Deposits Generated from FEBID of CF_3AuCNMe

CF_3AuCNMe

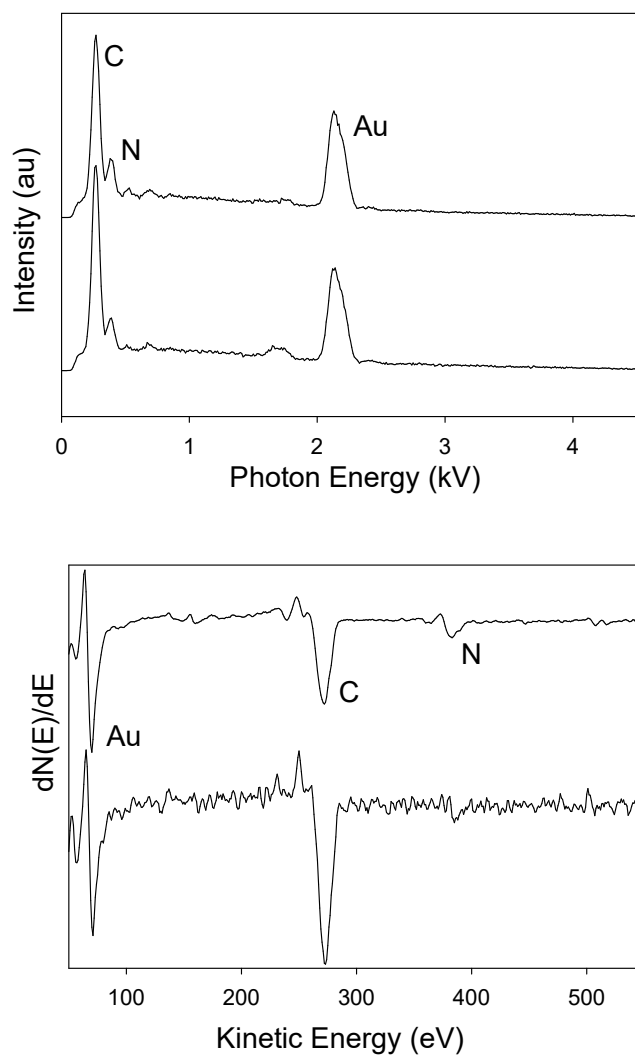


Figure S17. Comparison of (top) EDS data and (bottom) AES data acquired from deposits generated from CF_3AuCNMe .

References:

1. SHELXTL2014, (Bruker-AXS, Madison, Wisconsin, 2014).
2. I. Utke, P. Hoffmann and J. Melngailis: Gas-Assisted Focused Electron Beam and Ion Beam Processing and Fabrication. *J. Vac. Sci. Technol., B* **26**, 1197 (2008).